Mechanical characterization of the elastoplastic response of asphalt felt paper

Article *in* Composites Part B Engineering · May 2017

DOI: 10.1016/j.compositesb.2017.02.020

Mechanical characterization of the elastoplastic response of asphalt felt paper

Claudio A. Bustos[a], Claudio M. García–Herrera[a]*, Diego J. Celentano[b], Diego A. Vasco[a]

a: Departamento de Ingeniería Mecánica, Universidad de Santiago de Chile, USACH, Av. Bernardo O'Higgins 3363, Santiago de Chile, Chile
b: Departamento de Ingeniería Mecánica y Metalúrgica, Pontificia Universidad Católica de Chile, PUC, Av. Vicuña Mackenna 4860, Santiago de Chile, Chile

Abstract

A numerical and experimental analysis of the mechanical response of asphalt felt paper is presented. This material is widely used as a moisture barrier in buildings made of light materials. To ensure such function, it is necessary for this material not to be torn during its installation and operation and, for this reason, it is important to know its mechanical behavior in detail. To that end, tensile and bulge tests were carried out and respectively used to characterize the in-plane and out-of-plane rate-independent elastoplastic material responses which were observed to be strongly dependent on the directions of the cellulose fibers. The constitutive model considers the anisotropic character of the material assuming the Hill-48 function to define both the yield surface and the non-associated plastic flow rule to properly predict the mechanical behavior for the full deformation ranges of both tests. The procedure to fit the material parameters is carried out via a proposed iterative numerical-experimental methodology. The obtained results are found to adequately describe the material response in both the tensile and bulge tests.

Keywords: Paper; Paperboard; Plasticity; Anisotropy; Mechanical characterization.

1 INTRODUCTION

Asphalt felt paper (asphalt saturated kraft paper or building paper) was manufactured for the first time in the 1950s, and it is extensively used at present due to its unique qualities. Its main function is to provide a protective layer that resists outdoor conditions (i.e., as weather

*Corresponding author: claudio.garcia@usach.cl

resistive barrier, WRB) and maintains the integrity of the internal structures of a building, protecting them against moisture either on roofs or walls (Butt, 2005).

The felt manufacturing process begins by preparing the asphalt (blowing process) and follows with a series of stages in which the base felt is impregnated by saturating it with asphalt (U.S. Environmental Protection Agency, 2001). In the specific case of asphalt felt, the raw material is kraft pulp, preferably the unbleached basic grades, which are more resistant (Butt, 2005). One of these is Grade D which comes from virgin wood and is characterized by its lower weight and thickness (Fortifiber, 2007; Holladay, 2000). Currently, this is the most widely used kind due to its easier installation and lower cost and, therefore, it is commonly utilized under stucco or stone finishes on wooden surfaces (Holladay, 2013).

Asphalt felt has a number of advantages, such as good resistance to damage and temperature fluctuations, low water permeance, low cost and successful use history, making it ideal as a moisture-proofing barrier. However, it is deficient in some aspects, e.g., it has low tearing resistance and it is affected negatively by too long exposures to water and air. An eventual fault as a result of a tear during its installation or due to an internal requirement along its operation life hinders its function severely.

Regarding to the mechanical behavior of the felt, the response is derived mostly from its structure and arrangement of the cellulose fibers of the kraft paper. In general, paper has a complex anisotropic behavior. Paper basically consists of a dense matrix of pores and intertwined fibers, with a mean fiber length of 2.1 mm and a width of 30 μm (Alava and Niskanen, 2006). During the paper manufacturing process, the cellulose fibers suspended in water are sprayed by a head box on an endless plastic fabric (wire), where the paper sheet is dehydrated, pressed and dried to form the links between the fibers. Due to this movement and the stiffness of the fibers, they tend to become aligned on the plane and preferentially in the machine direction (Mäkelä and Östlund, 2003).

To date, most mechanical tests applied for the characterization of paper have been based on uniaxial tests in the assumed symmetry material directions that define three orthogonal planes according to the paper manufacturing process, i.e., the machine, cross-machine and thickness directions. The orthotropic properties of the material may be determined in this way by considering an uncoupled influence of the different in-plane directions. This material is typically loaded in its plane and, therefore, it is possible to neglect its response through the thickness, thereby greatly simplifying the experimental work and, in turn, the constitutive model used to describe it (Stenberg, 2001). Aside from tensile tests, it is also convenient to carry out structural tests that account for the simultaneous behavior of the fibers in both the machine and cross-machine directions. A clear example of this is the bulge test which is, in

general, applied to thin sheets (Lăzărescu et al., 2012). Its advantage is that it provides a biaxial stress state where the anisotropic behavior in the plane is developed completely and, in this way, it is possible to realistically complement the material response observed in this test with those of the tensile tests. More recently, Bolzon and Talassi (2014) carried non-conventional inflation tests on paperboard in order to study the behavior up to failure under the loading condition more commonly experienced by this material in industrial applications (e.g., beverage packaging). However, it is recognized the need of extensive experimental work for the three-dimensional calibration of the material, particularly for the response through the thickness.

For a representative volume, paper shows a homogeneous behavior, but dependent on the load direction. Based on its distinct responses observed along the machine, cross-machine and thickness directions, some orthotropic constitutive models have been recently proposed for this material. Xia et al. (2002) and Mäkelä and Östlund (2003) have developed elastoplastic models under this hypothesis, extending them also to the behavior of the paperboard. They characterize the anisotropic behavior accounting for linear elastic and plastic deformations, anisotropic hardening, and non-quadratic yield functions, restricting them to the case of associated flow rules. Bolzon and Talassi (2014) used an orthotropic linear elastic and associated Hill-48 plastic models to analyze the paperboard behavior under the assumption of plane stress condition using shell finite elements. Borgqvista et al. (2014, 2015) proposed an anisotropic elastoplastic continuum model for paperboard that considers the different in-plane and out-of-plane material behaviors through an energy density function defined in the spatial configuration. It should be noted that these models have not been characterized to the asphalt felt paper.

In the present work, we propose to perform the mechanical characterization of the asphalt felt paper through an infinitesimal-strain rate-independent elastoplastic model that assumes orthotropy for both the elastic and plastic responses. The Hill-48 function is considered for the definitions of the yield surface, in which a Hollomon-type hardening law is used, as well as for the non-associated flow rule of plastic deformation. The objective of this study is twofold: firstly, in view of the scanty data provided by the manufacturers of asphalt felt, to obtain experimental information of the mechanical response of this material and, secondly, to perform numerical simulations aimed at describing such behavior thus allowing to predict its performance in applications where its integrity, as mentioned above, is critical. To that end, uniaxial tensile tests in different orientations together with the bulge test have been carried out to calibrate, from the observed in-plane and out-of-plane experimental measurements, the material parameters of the adopted constitutive model. Section 2 describes the materials and

methods used while the experimental and numerical results given in Section 3 are discussed in Section 4. Finally, the concluding remarks are drawn in Section 5.

2 MATERIALS AND METHODS

2.1 EXPERIMENTAL PROCEDURE

2.1.1 MATERIALS

The material used for the mechanical tests corresponds to a commercial felt composed of kraft paper impregnated with asphalt, which is of the smooth type and has a black color. It has a weight of 198.43 ± 0.04 gr/m^2 and a thickness of 0.26 ± 0.01 mm. Test samples according to TAPPI T400 and T494 standards are obtained, consisting of rectangular strips 180 ± 5 mm effective length and 25 ± 1 mm width.

Since this material, the same as paper, has an anisotropic behavior in the plane, three orthogonal planes are commonly defined, namely the machine direction (MD, x-axis), the cross-machine direction (CD, y-axis) and the thickness direction (ZD, z-axis). Figure 1 illustrates the extraction directions for the uniaxial tensile test, which will be applied to the MD and CD samples and, in addition, to the diagonal direction (DD, i.e., 45° sample between MD and CD) sample as well. Furthermore, circular samples with a diameter of 70 mm were cut for the bulge test.

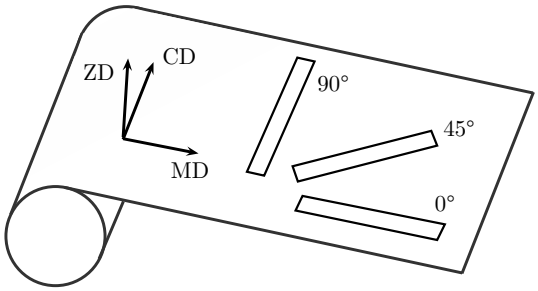

Figure 1: Main directions of the felt and extraction directions of the analyzed tensile samples.

2.1.2 UNIAXIAL TENSILE TEST

The main objective of this test is to determine the stress-strain relationship by subjecting the material to a uniaxial load condition. The advantage of this test is its simplicity since,

by recording simultaneously the force and the extension between the grips, it leads to the determination of the in-plane mechanical response.

Figure 2 shows the setup for the tests performed on an Instron 3324 tensile machine. A low load cell speed value of 2.5 mm/min was used to preclude rate-dependent effects. The tests were carried out under ambient conditions of 20 ^{o}C and 60% relative humidity, recording the force and displacement of the grips with a precision of 0.01 N and ± 1 μm, respectively. Pneumatic grips were used for holding the test samples at a pressure of 40 psi (calibrated to minimize damage by squeezing). The load cell used in the testing machine has a maximum capacity of 500 N. Furthermore, an optical micrometer was mounted to record the transverse narrowing (w) of the sample with a precision of ± 50 μm. The data acquisition was calibrated to gather 10 data per second.

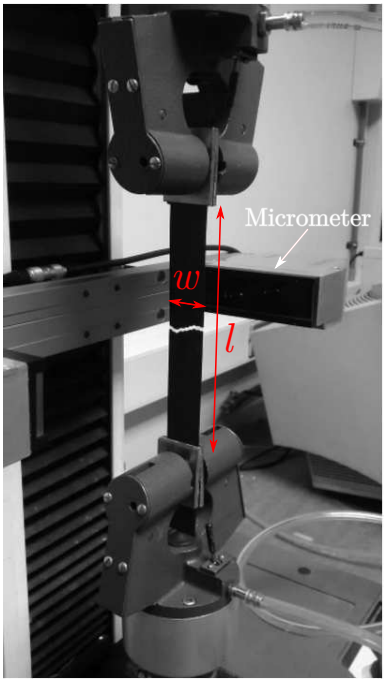

Figure 2: Setup of the tensile test.

In this test, the engineering stress and strains are respectively defined as $\sigma = P/a_0$ and $\varepsilon_{\text{axial}} = l/l_0 - 1$ and $\varepsilon_{\text{cross}} = w/w_0 - 1$, where P is the recorded axial force, a_0 is the initial cross section of the sample, l and w are the respective length and width measured during the test (subscript 0 refers to initial dimensions).

In addition, due to the anisotropy of this kind of material, the microstructure was analyzed by scanning confocal laser microscopy of samples that were not tested, with the purpose

of viewing the distribution of the in-plane fibers and correlating it with the mechanical performance seen in the uniaxial tensile test.

2.1.3 BULGE TEST

The bulge test consists in subjecting flat samples to a biaxial load condition by means of a pressurized fluid. Its objective is to determine the relationship between the internal pressure and the vertical displacement of the dome (bulge height), see Figure 3. The test involves a pressurizing chamber, a fixing system, and a data acquisition module. This kind of test is widely used in the characterization of thin sheets, usually considering the membrane theory of isotropic materials. One of its main advantages is that it does not present contact, so it avoids the frictional interaction that occurs in other forming tests.

For this work, we designed and made a device for circular samples that uses pressurized air as a fluid. A schematic of the pneumatic circuit and the experimental assembly are shown in Figure 3a. Discs of 70 mm in diameter were cut, leaving 14.5 mm for holding them. Therefore, the effective pressurization section has a diameter of 41 mm. The holding system considers a conical section (see Figure 3b) so that the sample levels with the upper surface allowing the vertical displacement to be recorded from the side. An O-ring is also included between the base and the flange to avoid pressure loss. The pressure was injected at a rate of 3 kPa/s in order to ensure a rate-independent response. During the whole test until rupture, the pressure and vertical displacement of the dome were respectively recorded by means of a digital transducer (± 0.02 kPa) and an optical micrometer (± 50 μm).

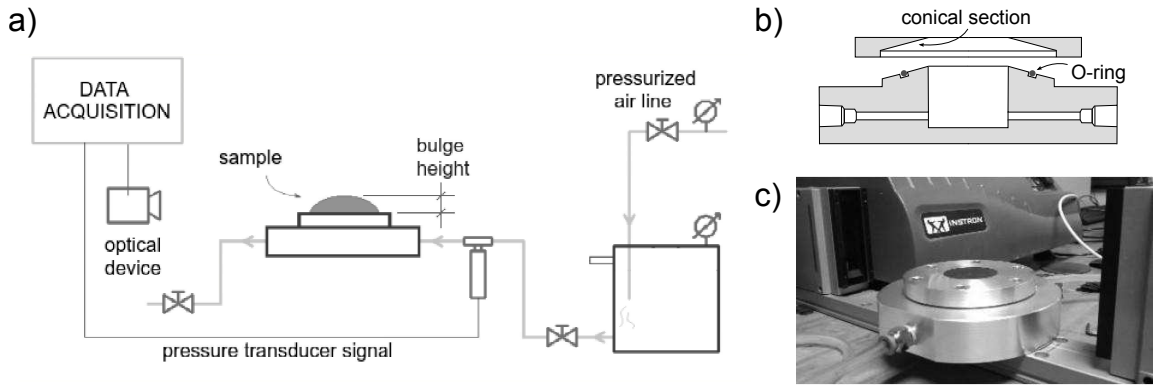

Figure 3: Experimental setup for bulge test. (a) Schematic of the pneumatic circuit, (b) cross section of the bulge device and (c) experimental assembly.

2.2 CONSTITUTIVE MODELLING

As already mentioned, an infinitesimal-strain rate-independent elastoplastic model that assumes orthotropy for both the elastic and plastic responses of the asphalt felt paper is proposed. The infinitesimal-strain theory is adopted due to the small deformation range exhibited by this material in the experimental measurements to be presented in Section 3.

In the material symmetry directions defined previously, the stress-strain law is written as:

$$\boldsymbol{\sigma} = \boldsymbol{D}(\boldsymbol{\varepsilon} - \boldsymbol{\varepsilon}^p) \tag{1}$$

where $\boldsymbol{\sigma}$ is the stress tensor, $\boldsymbol{D}$ is the orthotropic elastic constitutive tensor, $\boldsymbol{\varepsilon}$ is the strain tensor and $\boldsymbol{\varepsilon}^p$ is the plastic strain tensor. In this context, the inverse of $\boldsymbol{D}$ is given by:

$$\boldsymbol{D}^{-1} = \begin{bmatrix} 1/E_{xx} & -\nu_{yx}/E_{yy} & -\nu_{zx}/E_{zz} & 0 & 0 & 0 \\ -\nu_{xy}/E_{xx} & 1/E_{yy} & -\nu_{zy}/E_{zz} & 0 & 0 & 0 \\ -\nu_{xz}/E_{xx} & -\nu_{yz}/E_{yy} & 1/E_{zz} & 0 & 0 & 0 \\ 0 & 0 & 0 & 1/G_{xy} & 0 & 0 \\ 0 & 0 & 0 & 0 & 1/G_{xz} & 0 \\ 0 & 0 & 0 & 0 & 0 & 1/G_{yz} \end{bmatrix} \tag{2}$$

with $\nu_{yx}/E_{yy} = \nu_{xy}/E_{xx}$, $\nu_{zx}/E_{zz} = \nu_{xz}/E_{xx}$ and $\nu_{zy}/E_{zz} = \nu_{yz}/E_{yy}$., where E is the Young modulus, ν is the Poisson ratio and G is the shear modulus, all of them associated with the material symmetry directions.

The Hill-48 function, developed to express the yield surface for materials with orthotropic behavior, is defined in the following way:

$$f = \sqrt{F(\sigma_{yy} - \sigma_{zz})^2 + G(\sigma_{zz} - \sigma_{xx})^2 + H(\sigma_{xx} - \sigma_{yy})^2 + 2L\sigma_{yz}^2 + 2M\sigma_{zx}^2 + 2N\sigma_{xy}^2} - C^p = 0 \tag{3}$$

where the first term represents the equivalent stress, F, G, H, L, M and N are the Hill parameters and C^p is the hardening stress that can be written for a Hollomon-type law as:

$$C^p = A^p(\varepsilon_0^p + \varepsilon^p)^{n^p} \tag{4}$$

such that $\sigma_{\mathrm{MD}} = A^p(\varepsilon_0^p)^{n^p}$ is the yield stress in the machine direction, A^p and n^p are the hardening parameters and ε^p is the equivalent plastic strain. A particularization of Equation (3) for the case of plane stress adopted in this study ($\sigma_{zz} = 0$ and $\sigma_{yz} = \sigma_{zx} = 0$) takes the

following form:

$$f = \sqrt{\sigma_{xx}^2 + (F+H)\sigma_{yy}^2 - 2H\sigma_{xx}\sigma_{yy} + 2N\sigma_{xy}^2} - C^p = 0 \tag{5}$$

The rate-independent flow rule to describe the plastic strain increment is:

$$\dot{\boldsymbol{\varepsilon}}^p = \dot{\lambda}\frac{\partial g}{\partial \boldsymbol{\sigma}} \tag{6}$$

where $\dot{\lambda} > 0$ is the plastic consistency multiplier (computed using standard concepts of the plasticity theory) and g is the plastic potential function. Here we use the Hill-48 yield function as the plastic potential, but in principle with different parameters from those of f, thus resulting in a constitutive model with a non-associated flow rule. The parameters corresponding to f and g (i.e., F, G, H and N) are respectively denoted with subindexes f and g.

The least-squares fitting procedure aimed at deriving realistic elastic and plastic material parameters is presented below.

2.3 FITTING PROCEDURE

Due to the large number of parameters involved in the adopted elastoplastic model described in Section 2.2, the fitting methodology proposed to characterize the material response consisted in the use of a least–squares procedure applied to the experimental measurements and numerical results according to the following three steps which allow the independent derivation of both the in-plane and out-of-plane elastoplastic material parameters.

Step 1. In-plane fitting considering the MD and CD tensile test results.

The initial purely elastic deformation stage of the experimental tensile tests provided the elastic constants, such as the elastic moduli ($E_{xx} = \sigma_{xx}/\varepsilon_{xx}$ for MD and $E_{yy} = \sigma_{yy}/\varepsilon_{yy}$ for CD) and the Poisson's ratios ($\nu_{xy} = -\varepsilon_{yy}/\varepsilon_{xx}$ for MD and $\nu_{yx} = -\varepsilon_{xx}/\varepsilon_{yy}$ for CD, checking that the condition $\nu_{yx}/E_{yy} = \nu_{xy}/E_{xx}$ was effectively fulfilled).

Furthermore, the yield stresses σ_{MD} and σ_{CD} were defined considering a difference of 1% with respect to the value lying on the line that adjusts the initial slope of the MD and CD tensile curves, respectively. It should be noted, however, that the definition of these values is not straightforward due to the small elastic strains involved which are particularly apparent in load-unload cycles (Castro and Ostoja-Starzewski, 2003).

This step also included the derivation, from the MD curve, of the Hollomon hardening

parameters A^p and n^p. In addition, assuming associativeness, the parameters F, G and H of the yield and plastic potential functions are derived in terms of the Lankford coefficients R_{MD} and R_{CD} as:

$$F_f = F_g = \frac{1}{1+R_{\mathrm{MD}}}\frac{R_{\mathrm{MD}}}{R_{\mathrm{CD}}} \tag{7}$$

$$G_f = G_g = \frac{1}{1+R_{\mathrm{MD}}} \tag{8}$$

$$H_f = H_g = \frac{R_{\mathrm{MD}}}{1+R_{\mathrm{MD}}} \tag{9}$$

where R_{MD} and R_{CD}, which quantify the degree of anisotropy according to the in-plane directions, are respectively obtained from the MD and CD tensile tests as the ratio of the plastic strain increments along the width and thickness of each sample:

$$R_{\mathrm{MD}} = \frac{\dot{\varepsilon}^p_{yy}}{\dot{\varepsilon}^p_{zz}} \quad ; \quad R_{\mathrm{CD}} = \frac{\dot{\varepsilon}^p_{xx}}{\dot{\varepsilon}^p_{zz}} \tag{10}$$

where $\dot{\varepsilon}^p_{zz}$ is computed from the plastic incompressibility condition ($\dot{\varepsilon}^p_{zz} = -\dot{\varepsilon}^p_{xx} - \dot{\varepsilon}^p_{yy}$). For the MD direction, this is given by $\dot{\varepsilon}^p_{zz} = -(\dot{\varepsilon}_{xx} - \dot{\sigma}_{xx}/E_{xx}) - (\dot{\varepsilon}_{yy} + \nu_{xy}\dot{\sigma}_{xx}/E_{xx})$ (similar expressions can be deduced for the DD and CD directions).

Among the hypotheses considered in this paper, it is assumed that the MD and CD samples undergo a homogeneous stress-strain state under an axial load (as commented below, note that this is not the case for the DD sample). Therefore, in the numerical simulations, the MD and CD tensile tests were simulated with only one hexahedral finite element for one fourth of the geometry. Figure 4a shows the boundary conditions, where w_0 is the width, l_0 the length, b_0 the thickness and u is the imposed displacement.

Step 2. In-plane fitting considering the DD tensile test results.

The yield stresses σ_{DD} was obtained from the DD tensile curve using the same procedure described above in Step 1.

The shear modulus G_{xy} is firstly estimated as (Castro and Ostoja-Starzewski, 2003):

$$G_{xy} = \frac{E_{xx}E_{yy}}{E_{xx}(1+\nu_{yx}) + E_{yy}(1+\nu_{xy})} \tag{11}$$

The parameter N of the yield and plastic potential functions is firstly computed as:

$$N_f = N_g = \frac{1 + 2R_{\mathrm{DD}}}{2} \frac{R_{\mathrm{MD}} + R_{\mathrm{CD}}}{R_{\mathrm{CD}}(1 + R_{\mathrm{MD}})} \tag{12}$$

such that the Lankford coefficient R_{DD} obtained from the DD tensile curve is defined as:

$$R_{\mathrm{DD}} = \frac{\dot{\varepsilon}^p_{y'y'}}{\dot{\varepsilon}^p_{zz}} \tag{13}$$

where the direction y' is the result of rotating the direction y by 45°.

Since non-homogeneous stress and strain patterns caused by the presence of the fibers are developed in this case, a finite element mesh composed of 2240 hexahedral elements with 4746 nodes was considered for the whole geometry. The boundary conditions are shown in Figure 4b.

As described in Section 3, the values given by equations 11 and 12 are initial guess such that the final derivation of G_{xy} and N was made by their sensitization until the the experimental elastoplastic in-plane behavior was adequately approached.

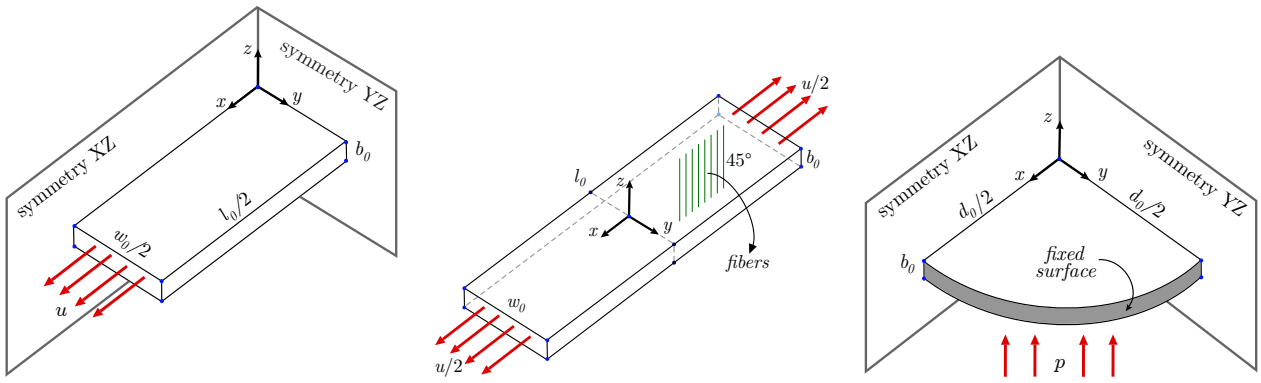

(a) (b) (c)

Figure 4: Representation of the boundary conditions for the (a) uniaxial tensile MD (CD is simply obtained replacing x by y and viceversa), (b) uniaxial tensile DD and (c) bulge tests.

Step 3. Out-of-plane fitting considering the bulge test results.

This step was mainly devoted to obtain the elastic parameters outside the plane because they do not play any role in the uniaxial tensile tests, i.e., E_{zz}, ν_{xz}, ν_{yz}, G_{xz} and G_{yz}. According to data reported in the literature (Xia et al. 2002), the following relationships are assumed: $E_{zz} = E_{xx}/300$, $\nu_{xz} = \nu_{yz} = \nu_{xy}/10$ and $G_{xz} = G_{yz}$.

The simulation of the bulge test was performed with a finite element model that consisted

of 2448 hexahedral elements with 3285 nodes for one fourth of the effective pressurized portion. The imposed boundary conditions are shown in Figure 4c, where p is a follow-up load that acts normal to the deformed surface. The analysis of the mechanical response was made by sensitizing the parameter G_{xz} until the experimental behavior was adequately approached.

The error for each step is quantified by means of the normalized root-mean-square deviation (NRMSD) in order to have a comparable value between the numerical and experimental curves. This parameter is given by:

$$\text{NRMSD} = \frac{1}{\Delta}\sqrt{\frac{1}{n}\sum_{i=1}^{n}(\hat{y}_i - y_i)^2} \tag{14}$$

where n is the number of experimental data, y_i is the experimental measurement, $\hat{y}_i$ is the numerical fitted value and $\Delta = |y_{max} - y_{min}|$.

3 RESULTS

3.1 TENSILE TEST

Figure 5 shows the cellulose fibers present in the asphalt felt paper studied in this work. They are oriented mostly in the machine direction with a mean diameter of 47.0 ± 5.4 μm. As shown below, their distribution strongly influences the global mechanical response of this material.

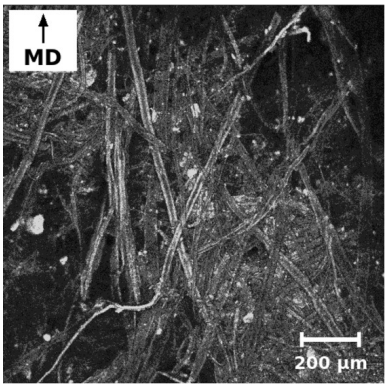

Figure 5: Cellulose fibers present in the felt as shown by scaning confocal laser microscopy.

Table 1 shows the average Lankford coefficient, yield stress and rupture strain and stress values determined in the tensile test for the three tested directions of the asphalt felt. Very

different responses along the three analyzed directions can clearly be appreciated where, as mentioned above, low strain levels are achieved in the material during the whole test. In particular, the negligible Lankford coefficient along DD is a unexpected result that was not previously reported in the literature for this material.

Direction	R	σ_{yield} [MPa]	ε_{rup}	σ_{rup} [MPa]
0° (MD)	0.987 ± 0.085	9.02 ± 0.88	0.017 ± 0.002	22.83 ± 1.681
45° (DD)	0.000 ± 0.005	3.89 ± 0.24	0.025 ± 0.003	12.98 ± 1.049
90° (CD)	0.115 ± 0.018	4.29 ± 0.14	0.029 ± 0.003	10.36 ± 0.433

± Standard deviation

Table 1: Lankford coefficient, yield stress and rupture strain and stress values obtained in the tensile test for the asphalt felt.

The numerical results fitted to the experimental measurements of the tensile tests using the equations of Step 1 described in Section 2.1.2 are plotted in Figure 6, where the vertical bars indicate the standard deviation for a total of 15 samples for each test. Table 2 shows the derived material parameters associated with directions MD and CD.

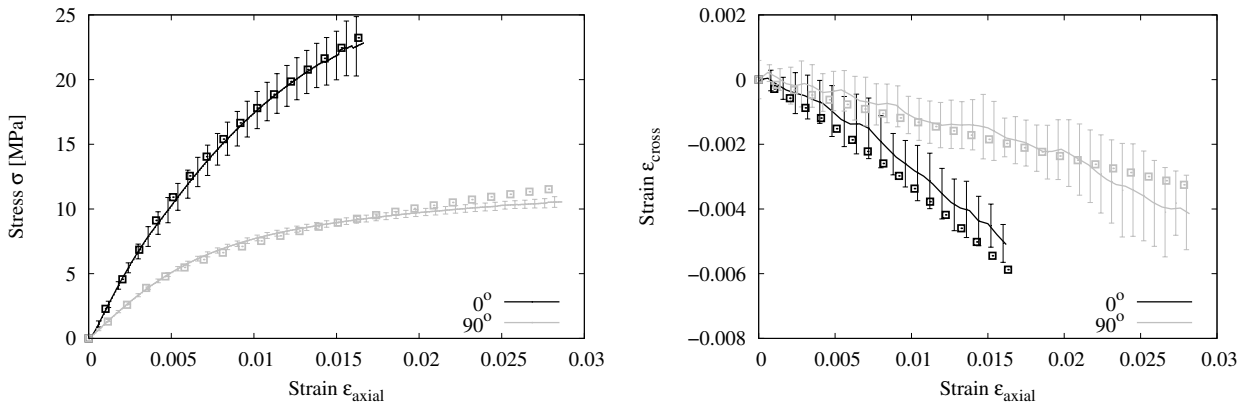

(a) Axial stress-strain

(b) Cross-axial strains

Figure 6: Comparison of experimental (lines) and numerical (dots) results in the MD and CD uniaxial tensile tests (Step 1).

From the experimentally measured values of the Lankford coefficients along the three directions shown in Table 1 and the elastic parameters included in Table 2, the shear modulus G_{xy} and the parameters N are obtained using equations 11 and 12, respectively. These values are respectively presented in Tables 3 and 4 (values corresponding to Iteration 0). The experimental measurements together with the numerical results of the tensile tests corresponding

Elastic parameters	
E_{xx} [GPa]	2.240
E_{yy} [GPa]	1.120
ν_{xy}	0.140
ν_{yx}	0.070
Hardening parameters	
σ_{MD}	9.02
A^p [MPa]	103.34
n^p	0.294
f and g parameters	
$F_f = F_g$	4.3090
$G_f = G_g$	0.5034
$H_f = H_g$	0.4966

Table 2: Fitted elastic, hardening and yield and plastic potential functions parameters (Step 1).

to Step 2 described in Section 2.1.2 are plotted in Figure 7 and 8. These results make clearly apparent that the associative model assumption is not able to properly capture the material response. Therefore, a two-stage iterative procedure aimed at deriving the shear modulus G_{xy} and the parameters N_f is performed. To this end, the normalized root-mean-square deviation is computed for both the uniaxial stress-strain and cross-axial strains curves (respectively denoted with subindexes USS and CAS). The final value of a parameter is adopted as that giving a relative variation of NRMSD between two successive iterations lower than 10%. First, the results varying G_{xy} are summarized in Table 3. It is seen that although the cross-axial strains curve is adequately fitted, relatively big numerical-experimental differences still remain for the stress-strain curve. Then, different values of N_f are used in order to minimize the numerical-experimental error in such curve. These values are shown in Table 4. The predicted curves obtained with the final values of N_f and G_{xy} shown in Figure 8 are seen to adequately describe the material response.

Iteration	G_{xy} [GPa]	$\text{NRMSD}_{\text{USS}}$	$\text{NRMSD}_{\text{CAS}}$
0	0.683	0.17739	1.89836
1	0.771	0.19371	1.18586
2	0.872	0.20882	0.60973
3	0.983	0.22243	0.48877

Table 3: NRMSD for different G_{xy} values (Step 2, stage 1).

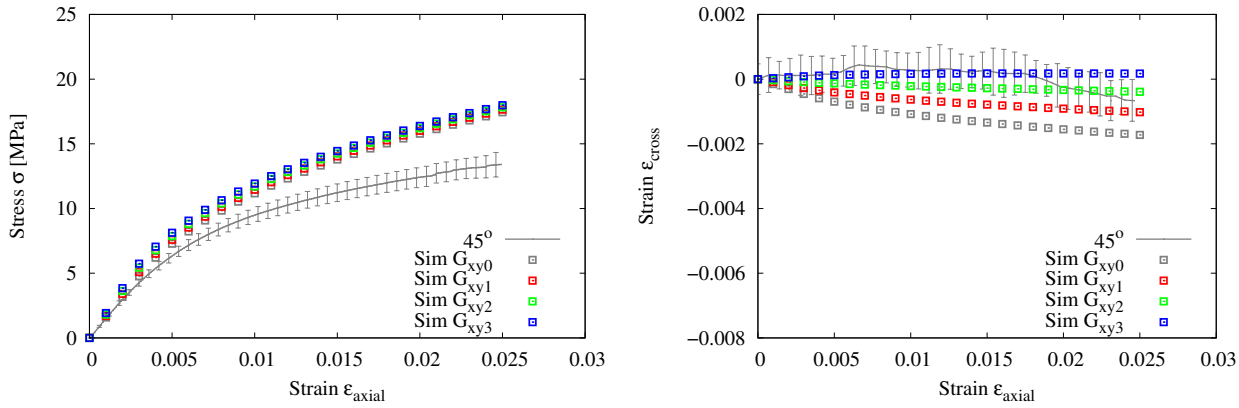

Figure 7: Comparison of experimental (lines) and numerical (dots) results in the DD uniaxial tensile test for different G_{xy} values (Step 2, stage 1).

Iteration	N_f	$\text{NRMSD}_{\text{USS}}$	$\text{NRMSD}_{\text{CAS}}$
0	2.4062	0.22243	0.48877
1	3.1281	0.15680	0.47927
2	4.0671	0.08811	0.46874
3	5.4059	0.02616	0.45845

Table 4: NRMSD for different N_f values (Step 2, stage 2).

Figure 9 presents the experimental measurements and numerical results for the final parameters for the axial stress-strain ($\sigma - \varepsilon$) and cross-axial strain ($\varepsilon_{\text{cross}} - \varepsilon_{\text{axial}}$) relationships.

3.2 BULGE TEST

The rupture stage in the bulge test was observed at a pressure of 138.84 ± 10.65 kPa with a maximum vertical displacement of the dome of 3.138 ± 0.116 mm.

Figure 10 shows the experimental measurements together with the numerical results for different values of $G_{xz} = G_{yz}$ summarized in Table 5. Subindex BT stands for the normalized root-mean-square deviation computed from this curve. Moreover, Table 6 shows all the resulting fitted parameters of the elastoplastic model presented in Section 2.2.

To appreciate the non-uniform stress pattern that results in the pole of the dome, Figure 11 shows the distribution of the principal stresses up to a pressure of 140 kPa seen from the XY plane. The directions of the stresses coincide with MD for σ_1 (x-axis) and CD for σ_2 (y-axis). The maximum values are located at the top of the dome, resulting $\sigma_1 = 23.67$ MPa

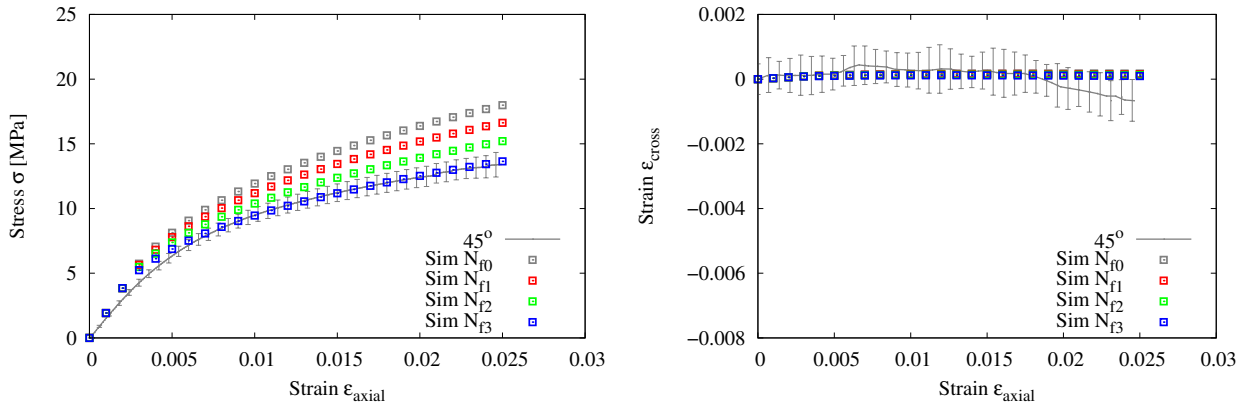

Figure 8: Comparison of experimental (lines) and numerical (dots) results in the DD uniaxial tensile test for different N_f values (Step 2, stage 2).

Iteration	$G_{xz} = G_{yz}$ [GPa]	NRMSD_{BT}
0	0.983	0.06662
1	1.228	0.05428
2	1.535	0.04275
3	2.000	0.03603

Table 5: NRMSD for different $G_{xz} = G_{yz}$ values (Step 3).

and $\sigma_2 = 10.89$ MPa.

4 DISCUSSION

An important aspect shown in Figure 6a is the difficulty in defining the yield stress due to the smooth transition between the elastic and elastoplastic regimes. The results show the strong orthotropic nature of both the elastic and plastic responses. In Figure 6b, it is seen that there is substantial strain variability with respect to the mean value. This is attributable to the non-uniform thickness along the samples. The initial slopes in MD and CD are around -0.50 and -0.15, respectively. This phenomenon has also been described by Xia et al. (2002), with the same value in MD and -0.13 in CD.

Figure 7a clearly shows that the stress-strain curve along DD is not affected by different values of the shear modulus G_{xy}. However, as depicted in 7b, they have a strong influence on the development of the cross strain which, according to the measurements, is practically zero during the whole deformation range. Conversely, it is seen in Figures 8a and 8b that the

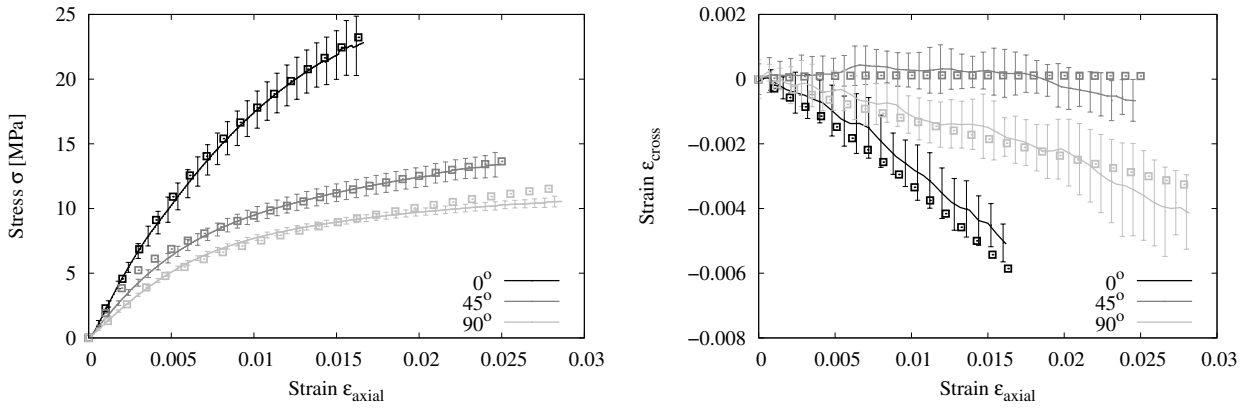

(a) Axial stress-strain

(b) Cross-axial strain

Figure 9: Comparison of experimental (lines) and final numerical (dots) results in the uniaxial tensile tests.

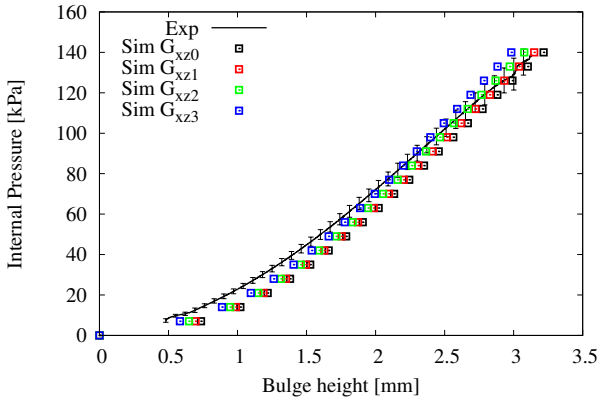

Figure 10: Comparison of the experimental (lines) and numerical (dots) results in the bulge test for different $G_{xz} = G_{yz}$ values (Step 3).

parameter N_f affects the stress levels but does not play any role in the transversal deformation. It should be mentioned that this characterization procedure is robut since the same values for G_{xy} and N_f are obtained if the two stages of Step 2 are inverted.

The associated and non-associated characters respectively found for parameters $F-G-H$ and N can be explained by their alternative estimation in terms of the yield stress values as (Banabic, 2010):

$$F_f = \frac{\sigma_{\mathrm{MD}}^2}{2}\left(\frac{1}{\sigma_{\mathrm{CD}}^2} + \frac{1}{\sigma_{\mathrm{b}}^2} - \frac{1}{\sigma_{\mathrm{MD}}^2}\right) \tag{15}$$

Elastic parameters	
E_{xx} [GPa]	2.240
E_{yy} [GPa]	1.120
E_{zz} [GPa]	0.004
G_{xy} [GPa]	0.983
$G_{xz} = G_{yz}$ [GPa]	2.000
ν_{xy}	0.140
$\nu_{xz} = \nu_{yz}$	0.014
Hardening parameters	
σ_{MD} [MPa]	9.02
A^p [MPa]	103.34
n^p	0.294
f and g parameters	
$F_f = F_g$	4.3090
$G_f = G_g$	0.5034
$H_f = H_g$	0.4966
N_f	5.4059
N_g	2.4062

Table 6: Final fitted elastic, hardening and yield and plastic potential functions parameters.

$$G_f = \frac{\sigma_{\mathrm{MD}}^2}{2}\left(\frac{1}{\sigma_{\mathrm{MD}}^2} + \frac{1}{\sigma_{\mathrm{b}}^2} - \frac{1}{\sigma_{\mathrm{CD}}^2}\right) \tag{16}$$

$$H_f = \frac{\sigma_{\mathrm{MD}}^2}{2}\left(\frac{1}{\sigma_{\mathrm{MD}}^2} + \frac{1}{\sigma_{\mathrm{CD}}^2} - \frac{1}{\sigma_{\mathrm{b}}^2}\right) \tag{17}$$

$$N_f = \frac{\sigma_{\mathrm{MD}}^2}{2}\left(\frac{4}{\sigma_{\mathrm{DD}}^2} - \frac{1}{\sigma_{\mathrm{b}}^2}\right) \tag{18}$$

where σ_{b} is the biaxal yield stress that can be estimated as:

$$\sigma_{\mathrm{b}} = \sigma_{\mathrm{MD}}\left(\frac{1}{1+R_{\mathrm{MD}}}\frac{R_{\mathrm{MD}}}{R_{\mathrm{CD}}} + \frac{1}{1+R_{\mathrm{MD}}}\right)^{-\frac{1}{2}} \tag{19}$$

The resulting yield function parameters (computed with $\sigma_{\mathrm{b}} = 4.11$ MPa) are summarized in Table 7. It is seen that these values are respectively comparable with those included in Table 6. Their difference can be attributable to the approximation considered to obtain σ_{b}.

Overall, Figure 9 shows that the numerical results computed with the material parameters summarized in Table 6 compare quite well with the experimental measurements for the three directions for the whole deformation range of the tensile test.

Unlike the works developed by Xia et al. (2002) and Bolzon and Talassi (2014) in which the

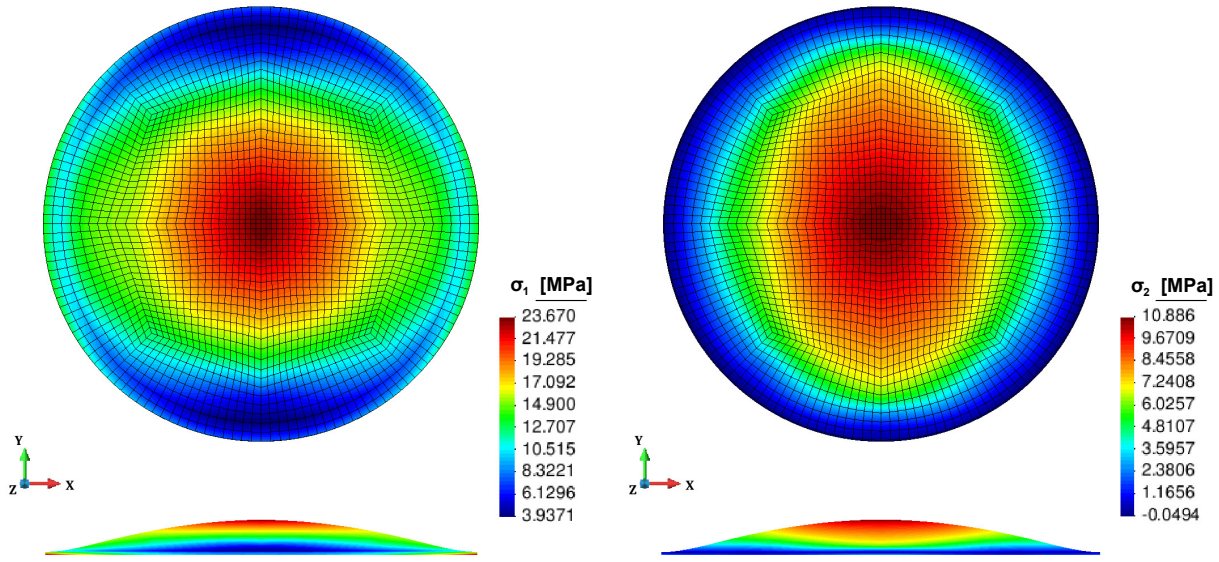

Figure 11: Distribution of the principal stresses σ_1 and σ_2 [MPa] in the simulation of the bulge test in the XY plane at a pressure of 140 kPa.

f parameters	
F_f	4.1217
G_f	0.7009
H_f	0.2991
N_f	8.3420

Table 7: Yield function parameters obtained in terms of the yield stress values.

material was exclusively carried out via tensile stress-strain curves, the iterative methodology applied in the present research not only incorporates the cross-axial strain curves but also the biaxial response resulting from the bulge test. This test provides relevant information on the mechanical response of the material since it is subjected to a complex load state activating all the stress and strain components in the adopted orthotropic model. The effect of the through-thickness shear caused by bending should not be relevant in this case due the sample slenderness considered in the test. The important role of the out-of-plane shear moduli could be attributable to the out-of-plane fiber dispersion which may generate a stronger fiber-matrix interaction compared to that corresponding to a pure plane fiber distribution. Figure 10 presents an excellent experimental-numerical match.

Figure 11 shows the distribution of the principal stresses up to the rupture pressure for the bulge test (140 kPa). It is seen that there is a non-uniform state for the stresses, forming

ellipses around the maximum point of the dome (central point). Considering the values of the principal stresses, the anisotropy presented by the material is shown, getting to more than twice in MD. Furthermore, its magnitude corresponds to the rupture limits shown in Table 1, with an error of 9.4% for the MD and 7.5% for CD.

The results shown in this work demonstrate that the quadratic Hill-48 function under the infinitesimal strain assumption is valid to achieve a realistic description of the elastoplastic response of asphalt felt paper.

5 CONCLUSIONS

The elastoplastic response of felt paper has been characterized. Its mechanical behavior in the tensile and bulge tests was analyzed considering an orthotropic non-associated model based on the Hill-48 function.

One of the main difficulties of the experimental work was derived from the low levels of both plastic and elastic deformations, as well as from the fact that the thickness of the samples is not constant, leading to distortions in the measurement of the Poisson coefficients. On the other hand, it is seen that the plasticity model depends on a large number of parameters that make the calibration procedure difficult to define completely the elastoplastic anisotropic behavior exhibited by the material.

An iterative numerical-experimental methodology was proposed to fit the parameters of the constitutive model. In the tensile test, the obtained results showed an adequate fit of the stress-strain relationship where the main differences lied in the cross-axial deformation curve corresponding to the CD samples. Moreover, in the bulge test the mechanical behavior was completely satisfactory during the whole deformation levels, thus validating the calibration procedure together with the adopted constitutive model.

However, it will be necessary in future research to validate and complement the experimental results with tests that subject the material to: a) out-of-plane load states to observe the behavior through the thickness, b) evaluation of non quadratic pressure-dependent yield functions c) assessment of rate-dependent effects on the material response to deal with unloading and higher strain rate situations, d) compressive stress states and e) tearing conditions.

6 CONFLICTS OF INTEREST

The authors have no conflicting interests regarding this paper.

7 ACKNOWLEDGEMENTS

The authors acknowledge with thanks the support through Proyectos Basales and the Vicerrectoría de Investigación, Desarrollo e Innovación of the Universidad de Santiago de Chile and Proyectos Basales USA1555.

8 REFERENCES

Alava, M. and Niskanen, K. 2006. The physics of paper. Report on Progress in Physics 69, 669-723.

D. Banabic (2010). Sheet Metal Forming Processes: Constitutive Modelling and Numerical Simulation. Springer-Verlag, Berlin.

Bolzon, G. and Talassi, M. 2014. A combined experimental and numerical study of the behaviour of paperboard composites up to failure. Composites: Part B 66, 358-367.

Borgqvista, E., Lindström, T., Trydingb, J., Wallina, M. and Ristinmaaa, M. 2014. Distorsional hardening plasticity model for paperboard. International Journal of Solids and Structures 51, 2411-2423.

Borgqvista, E., Wallina, M., Ristinmaaa, M., and Trydingb, J. 2015. An anisotropic in-plane and out-of-plane elasto-plastic continuum model for paperboard. Composites Structures 126, 184-195.

Butt, T. K. 2005. Water resistance and vapor permeance of wheater resistive barriers. Journal of ASTM International 10(2), 1-15.

Castro, J. and Ostoja-Starzewski, M. 2003. Elasto-plasticity of paper. International Journal of Plasticity 19, 2083-2098.

Fortifiber. 2007. Forti-Facts: Roofing felt fail to make the grade. A Technical bulletin from The Fortifiber Building System Group. Retrieved from `http://www.fortifiber.com/ask_vs_felt.html`.

Holladay, M. 2000. Choosing a sheathing wrap: What you need to know to choose asphalt felt, building paper or plastic housewrap. Journal of Light Construction, 1-9.

Holladay, M. 2013, September 18. All about water-resistive barriers. Retrieved from http://www.greenbuildingadvisor.com/blogs/dept/musings/all-about-water-resistive-barriers.

Lăzărescu, L., Comşa, S., Nicodim, I., Ciobanu, I. and Banabic, D. 2012. Characterization of plastic behaviour of sheet metals by hydraulic bulge test. Trans. Nonferrous Met. Soc. China 22, s275-s279.

Mäkelä, P. and Östlund, S., 2003 Orthotropic elastic-plastic material model for paper materials. International Journal of Solid and Structures 40, 5599-5620.

Stenberg, N., 2003 A model for the throught-thickness elastic-plastic behaviour of paper. International Journal of Solid and Structures 40, 7483-7498.

U.S. Environmental Protection Agency (EPA). 2001. Asphalt roofing and processing revised industry profile, Draft report. Retrieved from https://www3.epa.gov/ttnecas1/regdata/IPs/Asphalt%20Roofing_IP.pdf

Xia, Q. S., Boyce, M. C., Parks, D. M. 2002. A constitutive model for the anisotropic elastic-plastic deformation of paper and paperboard. International Journal of Solid and Structures 23(6), 269-276.